PAPER • OPEN ACCESS

Electron thermalization and ion acceleration in XUV-produced plasma from nanoparticles in He gas environment

To cite this article: Eva Klimešová *et al* 2025 *New J. Phys.* **27** 013004

View the article online for updates and enhancements.

New Journal of Physics

The open access journal at the forefront of physics

PAPER

OPEN ACCESS

Electron thermalization and ion acceleration in XUV-produced plasma from nanoparticles in He gas environment

Eva Klimešová[1,*] , Olena Kulyk[1], Lucas J Martin[1], Bernd Schütte[2] , Ulrike Frühling[3] , Markus Drescher[4,5], Rui Pan[3], Nikola Stojanovic[6], Ivette J Bermudez Macias[3,7], Stefan Düsterer[3] , Jakob Andreasson[1] , Marek Wieland[4,5] and Maria Krikunova[1,8]

1 ELI Beamlines facility, The Extreme Light Infrastructure ERIC, Za Radnicí 835, 252 41 Dolní Břežany, Czech Republic
2 Max-Born-Institut, Max-Born-Str. 2A, 12489 Berlin, Germany
3 Deutsches Elektronen-Synchrotron DESY, Notkestrasse 85, 22607 Hamburg, Germany
4 Institut für Experimentalphysik, Universität Hamburg, Luruper Chaussee 149, 22761 Hamburg, Germany
5 Center for Ultrafast Imaging, Luruper Chaussee 149, 22761 Hamburg, Germany
6 Institute for Optical Sensor Systems Deutsches Zentrum für Luft- und Raumfahrt, Rutherfordstrasse 2, 12489 Berlin, Germany
7 European XFEL GmbH, Holzkoppel 4, D-22869 Schenefeld, Germany
8 Wildau Technical University of Applied Sciences, Hochschulring 1, 15745 Wildau, Germany
* Author to whom any correspondence should be addressed.

E-mail: eva.klimesova@eli-beams.eu

Abstract

We use intense femtosecond extreme ultraviolet (XUV) pulses with a photon energy of 92 eV from the FLASH free electron laser to irradiate substrate-free CsCl nanoparticles surrounded by a He gas with a number density of around 10^{15} cm^{-3}. By simultaneously detecting electrons and energetic ions from the laser-irradiated micron-size target we study the acceleration mechanism of light ions at the microplasma-vacuum boundary as well as at the layer close to the nanoparticle surface. When the XUV pulse interacts with the gas alone, helium ions are accelerated to energies exceeding 100 eV. In the presence of the nanoparticle, light ions gain additional energy in the electric field around the ionized nanoparticle and their energy spectrum changes considerably. We present an electrostatic model to explain the ion acceleration mechanisms both with and without the nanoparticle and discuss the role of the gas environment in experiments.

1. Introduction

The development of free-electron lasers (FELs) delivering intense femtosecond pulses in the extreme ultraviolet (XUV) and x-ray domain has significantly advanced a number of research fields, ranging from photochemistry, atomic, molecular and optical sciences, to structural biology, condensed matter or plasma physics [1–4]. Among the main applications of FELs are investigations of substrate-free nanoscale targets (organic or inorganic) under intense XUV/x-ray irradiation. These include single-shot coherent diffractive imaging (CDI) of individual non-crystalline nanoscale objects, e.g. salt and sucrose nanoparticles [5, 6], cell organelles [7], cells [8], viruses [9] or metal nanocrystals [10, 11], and investigations of ultrafast phenomena in FEL-irradiated nanoscale systems, e.g. formation and dynamics of nanoplasma in rare-gas clusters either at XUV [12–17] or x-ray photon energies [18–22], enhanced absorption and multistep ionization in clusters [23, 24], ultrafast electron dynamics in single atomic clusters [25, 26], dynamic segregation of ion species in exploding heteronuclear clusters [27, 28], transient resonances in inorganic nanoparticles [6] or correlated electronic decay in complex systems [29–32].

In many of the investigations on substrate-free nanoscale targets, a free nanoparticle in vacuum interacting with the FEL pulse is considered. However, a gas environment can be present around the nanoparticle, either in the case of cluster beams surrounded by an uncondensed gas [33, 34] or for nanoparticles injected into a vacuum via an injector with an aerodynamic lens stack (ALS) [35–37]. Therefore, investigations of laser-irradiated nanoparticles in a gas atmosphere are highly relevant. In our previous work, we have studied interaction of intense NIR pulses with CsCl nanoparticles in a He gas

environment [38] and with only the gas environment [39]. The interaction of the target with the XUV pulse is different from the interaction with the NIR pulse. A strong NIR pulse removes a large part of electrons from the focal volume by the ponderomotive force [39], resulting in formation of a plasma channel in the focal volume. The plasma channel contains mainly unscreened positive charges. On the other hand, the main ionization mechanism by the XUV pulse is one-photon absorption and strong field effects can be neglected. Therefore, we expect that plasma produced in the focal volume of the XUV pulse remains quasi-neutral. Additionally, in a NIR-field irradiated nanoparticle, collisional heating and electron rescattering promote emission of energetic electrons from the nanoparticle [38], increasing the accumulated positive charge on the nanoparticle. Therefore, ion acceleration at the nanoparticle surface is mainly governed by repulsive Coulomb forces. Collisional heating and field-driven electron rescattering are not present in the XUV case.
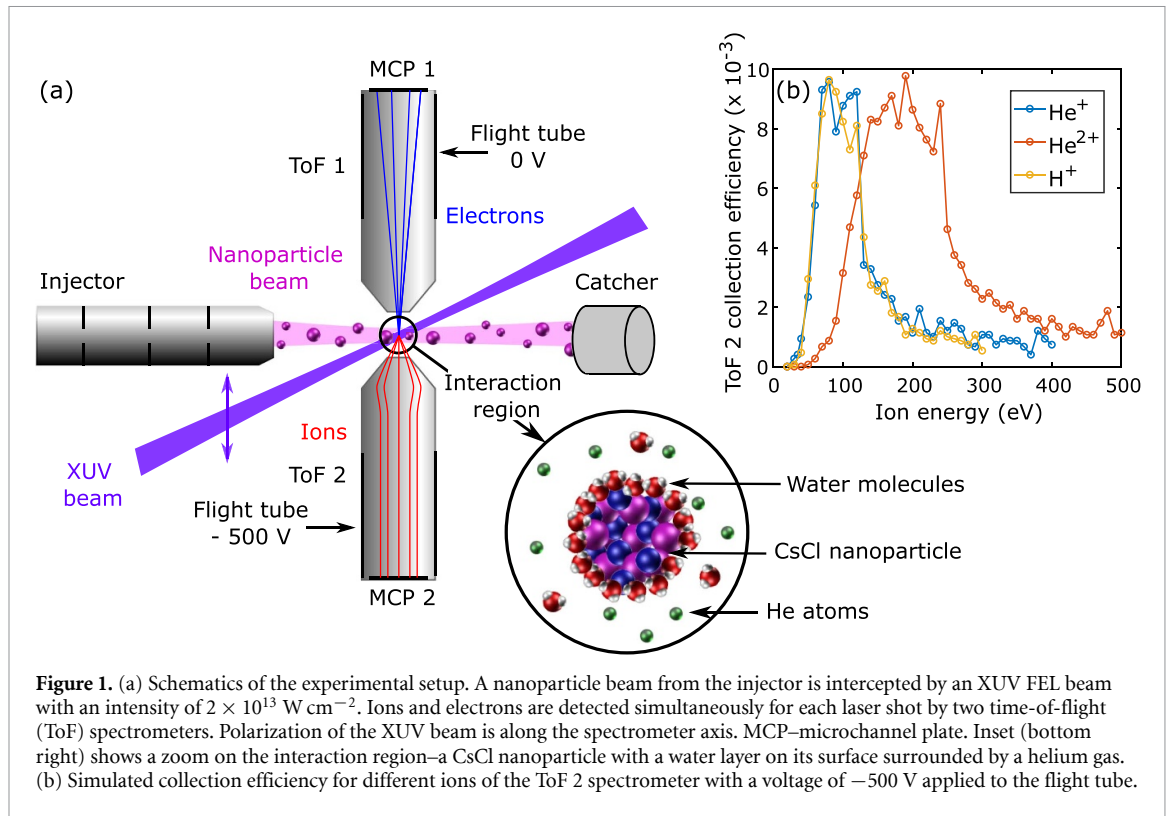
Understanding both NIR and XUV pulse interaction mechanisms is crucial, as it can help to develop novel pump-probe schemes. NIR/XUV pump-probe schemes have already been implemented in studies of XUV-induced [13, 17, 40, 41] and intense NIR-induced [42, 43] electron dynamics in molecules and clusters, as well as for time-resolved x-ray imaging of rare-gas clusters [15, 18, 22]. In these experiments both NIR and XUV pulses are strong enough to modify the target, therefore pump-probe signal depends on exact timing between XUV and NIR pulses [40].

In this work we investigate the interaction of intense XUV pulses (photon energy 92 eV) from the FLASH FEL in Hamburg with free CsCl nanoparticles in a helium gas environment. First, we show that in the FEL interaction with the gas of 10^{15} cm^{-3} density alone, a plasma is created, where ions are accelerated to energies on the order of 100 eV in the charge-separated layer at the plasma edge while electrons are slowed down. Second, when a CsCl nanoparticle in a gas environment interacts with the XUV pulse, the nanoparticle is ionized and the electric field around the nanoparticle leads to an additional acceleration of light ions. The gain in kinetic energy is around a factor of 2 higher than without the nanoparticle. Our spectroscopically-selective experiment together with a numerical model uncover electron and ion dynamics in XUV-produced microplasma and in the layer at the nanoparticle surface.

2. Experimental setup

The experiment was performed at the BL3 beamline of the FLASH FEL in Hamburg [44]. The FEL was operated at a repetition rate of 10 Hz in a single-bunch mode with an electron bunch charge of 0.3 nC, producing pulses with a central photon energy of around 92 eV and a full width at half maximum (FWHM) pulse duration of around 100 fs [45]. The mean energy per pulse was 0.1 mJ with estimated shot-to-shot variations of about 10%, as retrieved from the gas monitor detector data. The FEL beam was focused with a Mo/Si-coated spherical mirror (focal length 2 m) to a focal spot size with a diameter of $< 100\ \mu$m FWHM, resulting in a maximum intensity of 2×10^{13} W cm^{-2}. Zirconium filters or an aperture were used to adjust the pulse intensity. The FEL pulses interacted with a focused beam of CsCl nanoparticles from an aerosol nanoparticle injector [35] (figure 1(a)). In the injector, an aerosol was created from a 1% solution of CsCl in water using a gas dynamic virtual nozzle [46] and then delivered to the vacuum chamber via an ALS [36]. Helium was used as a carrier gas. On the way through the ALS most of the water from the aerosol droplets evaporated. However, because CsCl is highly hygroscopic, some remaining water molecules formed a layer at the nanoparticle surface [5, 47–49]. The mean diameter of CsCl nanoparticles was estimated to be around 400 nm using calculations of the droplet size from the nozzle [46] and comparisons with CDI measurements with a similar injector setup [5]. The approximate number density of nanoparticles was around 10^8 cm^{-3} and the estimated number density of He around the nanoparticle was on the order of 10^{15} cm^{-3} [39].

Ions and electrons from the interaction of the XUV pulse with the target were detected simultaneously on a single-shot basis using two time-of-flight (ToF) spectrometers placed perpendicularly to the laser and nanoparticle beams (figure 1(a)). The spectrometer axes were parallel to the polarization of the XUV beam. Both spectrometers were identical, consisting of a set of electrostatic lenses, a flight tube surrounded by a μ-metal shield and a 40 mm-diameter microchannel plate (MCP) detector with an anode [45, 50]. The signal from the anode was acquired with a 3.6 GHz digitizer. It was possible to apply a retardation voltage to the flight tube. The first spectrometer (ToF 1) was used to detect electrons in the drift mode. The second spectrometer (ToF 2) was used for a simultaneous ion detection. The volume around the interaction region was left field-free and a negative voltage of -500 V was applied to the flight tube of the ToF 2 spectrometer to accelerate ions towards the MCP detector. This allowed light ions, H$^+$, He$^+$ and He^{2+} with an initial kinetic energy larger than 40 eV, to reach the MCP, as confirmed by simulations with the SIMION software (version 8.1.1). In the simulations, trajectories of ions with different initial kinetic energies and initial directions were calculated. By counting the relative number of ions that reached the detector, the collection efficiency of the ion spectrometer was evaluated to be in the range from 1×10^{-3} up to 1×10^{-2} depending on the type and kinetic energy of the detected ions, see figure 1(b). Conversion of measured ToFs t to kinetic energies $\mathscr{E}_k$ of
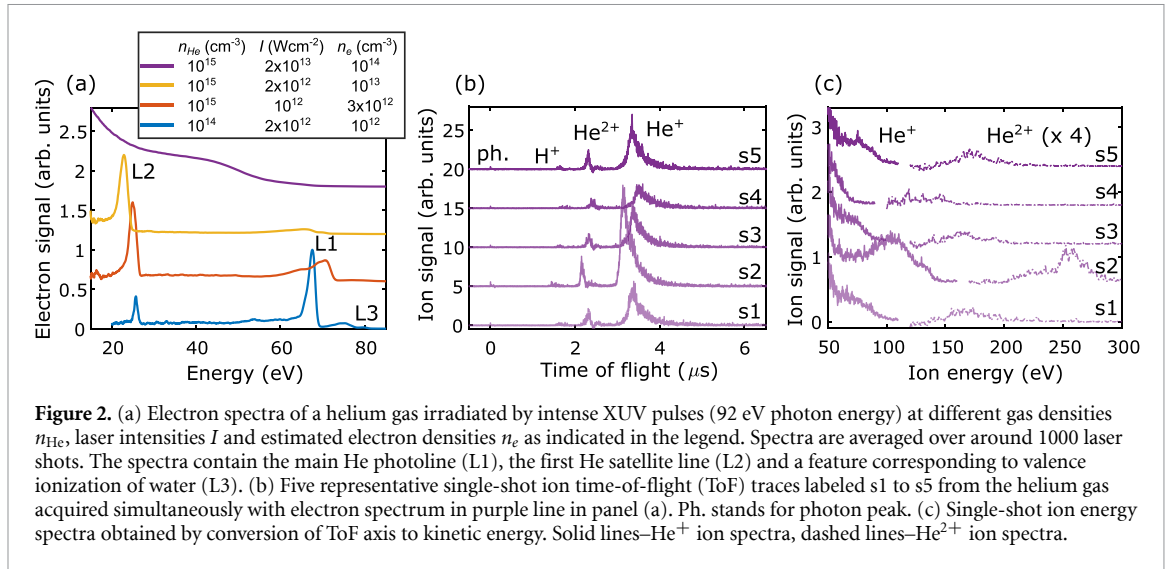
Figure 1. (a) Schematics of the experimental setup. A nanoparticle beam from the injector is intercepted by an XUV FEL beam with an intensity of 2×10^{13} W cm^{-2}. Ions and electrons are detected simultaneously for each laser shot by two time-of-flight (ToF) spectrometers. Polarization of the XUV beam is along the spectrometer axis. MCP–microchannel plate. Inset (bottom right) shows a zoom on the interaction region–a CsCl nanoparticle with a water layer on its surface surrounded by a helium gas. (b) Simulated collection efficiency for different ions of the ToF 2 spectrometer with a voltage of -500 V applied to the flight tube.

charged species was performed according to the relationship: $\mathscr{E}_k = a/(t-b)^2 + c$, where coefficients a, b and c were obtained from the SIMION simulation for each ion species. All measured ion spectra and yields were corrected for the spectrometer collection efficiency.

3. Electron and ion spectra from XUV-irradiated He gas

First, we study a microplasma formation in the focal volume of the XUV beam focused into the He gas from the injector by simultaneously measuring the electron and ion spectra for each FEL shot. Figure 2(a) shows averaged photoelectron spectra for different electron densities, obtained by varying gas number density n_{He} and/or the XUV intensity I. We assume single-photon absorption of He as a dominant process and estimate the resulting electron density n_e according to: $n_e = \sigma I \tau n_{He}/\hbar\omega$, where $\sigma = 0.5$ Mbarn is the ionization cross-section of He at 92 eV [51], τ is the pulse duration and $\hbar\omega$ is the photon energy. We estimate possible contribution of sequential two-photon double ionization of He to about 0.1% and single-photon double ionization of He to about 1.8% [51, 52]. These contributions are not taken into account in the estimations of electron number density.

From figure 2(a) we examine how electron spectra are altered with increasing electron density n_e in the focal volume. The spectrum obtained at the lowest electron density ($n_e = 10^{12}$ cm^{-3}, blue line in figure 2(a)) reflects the ionization of individual atoms. It contains the main photoline (labeled L1 in figure 2(b)) at 67 eV electron energy and the first satellite line (L2) at 27 eV created by a shake-up process, where a He$^+$ ion in the first excited state ($n = 2$) is created by a single-photon ionization [53, 54]. The broader peak L3 at energies of $73 - 80$ eV originates from ionization of valence shells of water molecules (binding energies 13 eV, 15 eV and 19 eV [55]). The measured intensity ratio between the first satellite line and the main photoline is around 0.4, which is larger than values from literature [51, 52]. Therefore, we believe, that although plasma is not created in the focal volume at the electron density of 10^{12} cm^{-3}, the L1, L2 and L3 lines are already shifted and broadened due to the accumulated space charge [56].

At estimated electron densities of 3×10^{12} to 10^{13} cm^{-3} (red and yellow lines in figure 2(a)), the relative intensity of the main helium photoline decreases, all lines are broadened and gradually shifted to lower kinetic energies. The change of relative intensities of L1 and L2 lines is an indication of a formation of a microplasma, where elastic and inelastic collisional processes take place. Photoelectrons from the main photoline are depleted by collisions with neutral He atoms and He$^+$ ions. The cross section of electron impact ionization of He atoms by a 67 eV electron is 32 Mbarn, while it is only 3 Mbarn for the 27 eV electron from the satellite line [57]. The cross section of electron impact ionization of He$^+$ ion by 67 eV electron is 1 Mbarn [57].

Figure 2. (a) Electron spectra of a helium gas irradiated by intense XUV pulses (92 eV photon energy) at different gas densities n_{He}, laser intensities I and estimated electron densities n_e as indicated in the legend. Spectra are averaged over around 1000 laser shots. The spectra contain the main He photoline (L1), the first He satellite line (L2) and a feature corresponding to valence ionization of water (L3). (b) Five representative single-shot ion time-of-flight (ToF) traces labeled s1 to s5 from the helium gas acquired simultaneously with electron spectrum in purple line in panel (a). Ph. stands for photon peak. (c) Single-shot ion energy spectra obtained by conversion of ToF axis to kinetic energy. Solid lines–He$^+$ ion spectra, dashed lines–He^{2+} ion spectra.

At the highest plasma density (10^{14} cm^{-3}, purple line in figure 2(a)), the electron kinetic energy distribution becomes smooth and structureless. This is a characteristic signature of thermalized electrons with near exponential kinetic energy distribution [30]. In this case we also investigate the ion spectra. Due to the configuration of our ion spectrometer, which has an optimized transmission for light ions within a certain kinetic energy range (figure 1(b)), ions can be detected only for the highest density case, where ion acceleration takes place. He$^+$ and He^{2+} ions with kinetic energies in the range of $40 - 350$ eV are observed (figures 2(b) and (c)). The He^{2+} ions can be generated by a single-photon double ionization [51, 54], by a two-photon sequential process [58] or by electron impact ionization [57]. As the probability of collisional interactions in thermalized plasma increases with increasing electron density, it is difficult to estimate, which process (XUV photon absorption or collisional interactions) contributes more to the formation of He^{2+} ions in the current study. The measured ion signal contains shot-to-shot fluctuations both in the yield and kinetic energy. Both fluctuations are attributed to shot-to-shot variations of the FEL pulse energy.
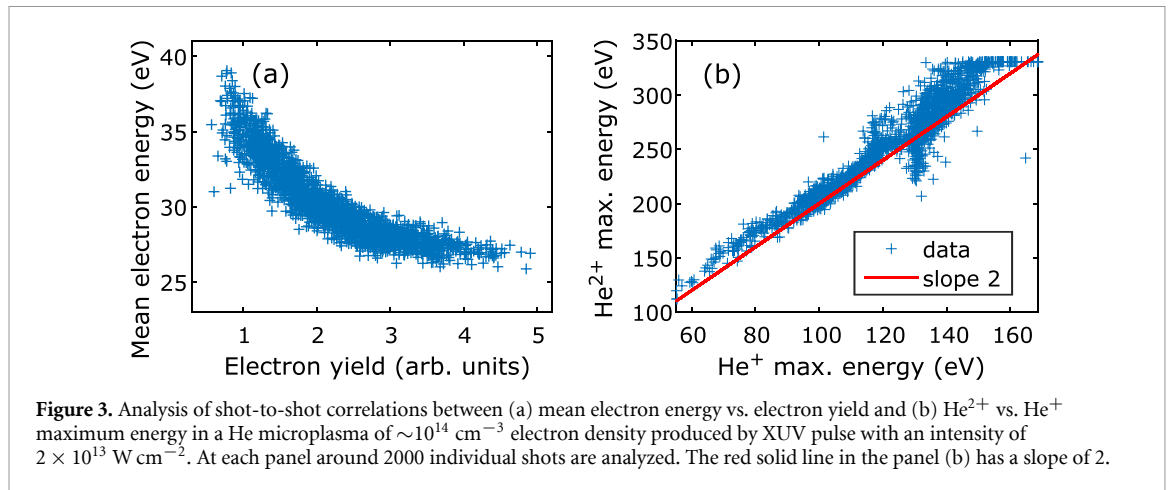
In figure 3 we analyze shot-to-shot correlations between electron yield and electron kinetic energy (panel (a)) and maximum kinetic energy of He^{2+} vs. He$^+$ signal (panel (b)). With increasing electron yield, that corresponds to an increase of electron density, the average electron kinetic energy decreases. This is indicative of more efficient electron thermalization in plasma caused by collisions with increasing electron plasma density. The measured single-shot He^{2+} maximum energies plotted versus He$^+$ maximum energies lie on a line with a slope of 2 (figure 3(b)), indicating that both ion species are accelerated in the same electric field. Thus, to evaluate ion kinetic energies we apply a plasma sheath model for a thermalized microplasma with electron density on the order of 10^{14} cm^{-3}. The electron density falls down at the plasma-vacuum boundary and a layer with separated charges (a sheath) is created [59, 60]. The width of the sheath is few Debye lengths, which is for our case few μm. This is much smaller than the focal spot diameter of 100 μm. Using the Bohm criterion, which assumes a balance between flux of electrons and ions in the thermalized plasma, the accelerating potential for ions across the sheath can be estimated according to [60]:

$$\phi = \frac{k_B T_e}{2e} \left[1 + \ln \left(\frac{m_i}{2\pi \langle Z \rangle m_e} \right) \right], \tag{1}$$

where k_B is the Boltzmann constant, T_e is the electron temperature, e is the electron charge, $\langle Z \rangle$ is the average ion charge and m_i, m_e are the ion or electron mass, respectively. An ion with a charge Ze can gain in this potential a maximum energy:

$$\mathcal{E} = Ze\phi. \tag{2}$$

To estimate helium ion energies in our experiment, we assume the average charge $\langle Z \rangle$ to be close to 1, as there are much more He$^+$ ions created either by photo- or electron impact ionization. The electron temperature $k_B T_e$ is estimated to be in the range of 20–40 eV from the measured average electron energy. By combining equations (1) and (2) we get He$^+$ maximum energies to be in the range of 80–160 eV and the He^{2+} maximum energies twice larger, which is in a good agreement with the measured values. Note, that the deviation of the measured single-shot He^{2+} maximum energies from the slope of 2 in figure 3(b) is caused

Figure 3. Analysis of shot-to-shot correlations between (a) mean electron energy vs. electron yield and (b) He^{2+} vs. He^+ maximum energy in a He microplasma of $\sim 10^{14}$ cm^{-3} electron density produced by XUV pulse with an intensity of 2×10^{13} W cm^{-2}. At each panel around 2000 individual shots are analyzed. The red solid line in the panel (b) has a slope of 2.

mainly by the drop of the spectrometer transmission for He^{2+} energies above 300 eV and the resulting large uncertainty in the determination of the fastest ToF and thus the maximum ion kinetic energy.

4. Electron and ion spectra from XUV-irradiated nanoparticles in He gas environment

When CsCl nanoparticles in a helium gas are irradiated by the FEL pulse, some laser shots hit the nanoparticle and some interact only with the carrier gas. In the analysis, individual laser shots are sorted to nanoparticle hits and misses according to the presence of an accelerated H^+ peak in the ion spectra (figures 4(a) and (b)). We suppose that the fast H^+ peak originates from the water layer at the nanoparticle surface [5, 47–49], because it is not present in shots without the nanoparticle and it is correlated to the photon peak (which is enhanced by scattering from the nanoparticle). The hit rate in the experiment is around 90%.
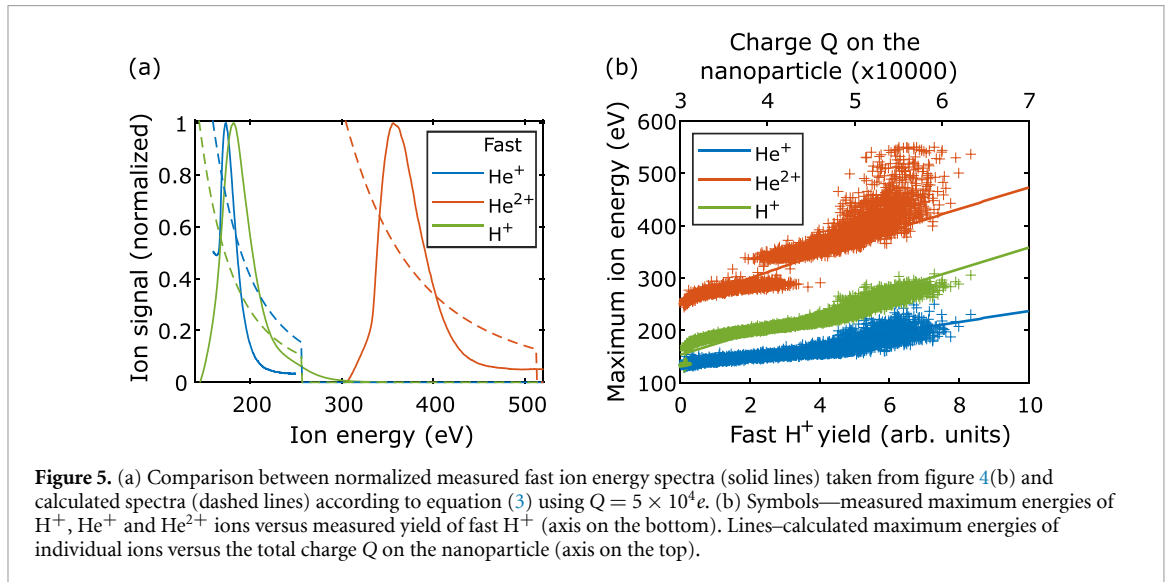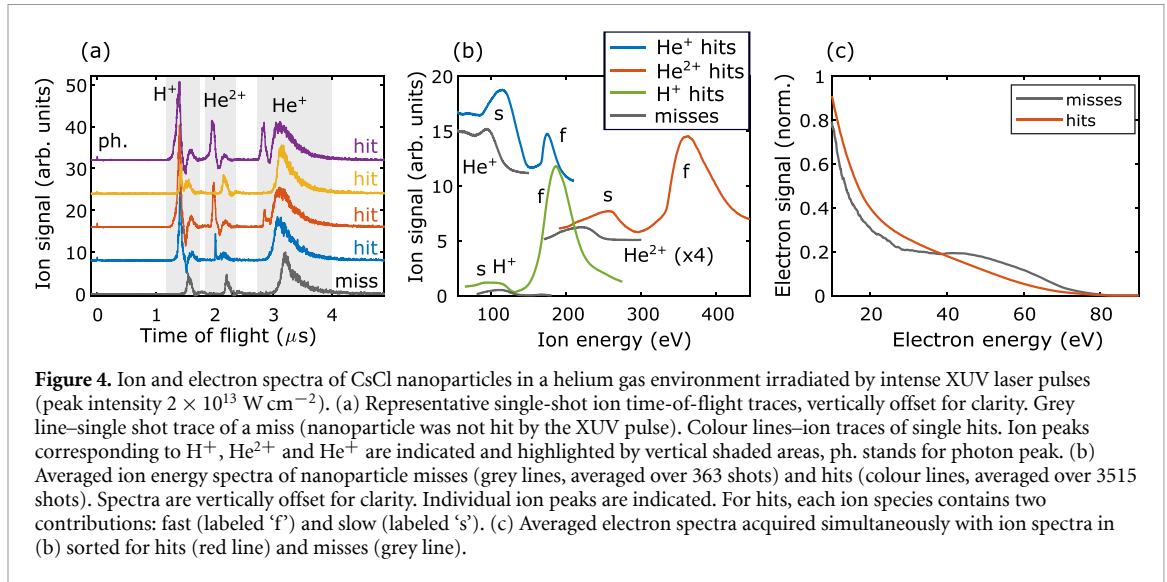
When the nanoparticle is hit, each of the detected H^+, He^+ and He^{2+} ion distributions typically contains two populations: slow, labeled 's', and fast, labeled 'f' in figure 4(b). When XUV pulse misses a nanoparticle, only slow ions are observed (figure 4(b)) and their spectra are very similar to ion spectra measured from the helium gas jet (figure 2(c)). Thus, we conclude that slow ions are accelerated in the plasma sheath at the microplasma-vacuum boundary, as discussed in section 3. Therefore, the energies of slow ions are not influenced by the presence of the nanoparticle. On the contrary, fast ions are detected while nanoparticle is hit by the FEL pulse. We attribute the pronounced shot-to-shot variations in the ion signal of hits (figure 4(a)) to the fluctuations of the nanoparticle position in the focal volume, the nanoparticle size and to energy fluctuations of the FEL beam [25, 26].

The electron spectra acquired simultaneously with ions and sorted for hits and misses are structureless (figure 4(c)), pointing to a production of a thermalized microplasma. Even for hits, electrons are mostly coming from the He microplasma, and contributions from individual atoms cannot be distinguished. The lower average energy of electrons in the case of hits compared to misses is attributed to a larger plasma density for hits as discussed in section 3 and figure 3(a).

Ion acceleration has been investigated for NIR-irradiated gas atmosphere with or without the nanoparticle [38, 39]. Here we apply a similar approach to the XUV regime, where we address acceleration of H^+ ions from the nanoparticle surface and He^+/He^{2+} ions from the gas around the nanoparticle. We start with a discussion of the ionization process and estimation of nanoparticle charging.

When a CsCl nanoparticle interacts with an intense XUV pulse with a photon energy of 92 eV, Cs atoms are ionized predominantly from the 4d shell (ionization cross-section 25 Mbarn [61]), followed by single and double Auger decay, leading to emission of electrons in the energy ranges of $32 - 40$ eV and below 20 eV [62, 63]. Cl atoms are ionized from the 3p and 3 s shells, leading to emission of electrons with $75 - 79$ eV kinetic energy. The kinetic energies of electrons emitted from outer valence orbitals of water are in the range of $73 - 80$ eV.

By the ionization of individual atoms within the nanoparticle, a large number of electrons are photoactivated. However, only small portion of ionized electrons can escape the Coulomb potential. Indeed, electron emission from the nanoparticle leads to the accumulation of the positive charge $Q = eN_{out}$ on the nanoparticle. Here, N_{out} is the number of escaped electrons. This mechanism is well understood from investigations of clusters in XUV fields [12, 24, 64], where nanoplasma formation has been studied. To estimate the number N_{out} of electrons that leave the nanoparticle, we compare the electron kinetic energy

Figure 4. Ion and electron spectra of CsCl nanoparticles in a helium gas environment irradiated by intense XUV laser pulses (peak intensity 2×10^{13} W cm^{-2}). (a) Representative single-shot ion time-of-flight traces, vertically offset for clarity. Grey line–single shot trace of a miss (nanoparticle was not hit by the XUV pulse). Colour lines–ion traces of single hits. Ion peaks corresponding to H$^+$, He^{2+} and He$^+$ are indicated and highlighted by vertical shaded areas, ph. stands for photon peak. (b) Averaged ion energy spectra of nanoparticle misses (grey lines, averaged over 363 shots) and hits (colour lines, averaged over 3515 shots). Spectra are vertically offset for clarity. Individual ion peaks are indicated. For hits, each ion species contains two contributions: fast (labeled 'f') and slow (labeled 's'). (c) Averaged electron spectra acquired simultaneously with ion spectra in (b) sorted for hits (red line) and misses (grey line).

Figure 5. (a) Comparison between normalized measured fast ion energy spectra (solid lines) taken from figure 4(b) and calculated spectra (dashed lines) according to equation (3) using $Q = 5 \times 10^4 e$. (b) Symbols—measured maximum energies of H$^+$, He$^+$ and He^{2+} ions versus measured yield of fast H$^+$ (axis on the bottom). Lines–calculated maximum energies of individual ions versus the total charge Q on the nanoparticle (axis on the top).

with the Coulomb potential barrier on the nanoparticle [64]. Considering the most energetic electrons have kinetic energy of 80 eV, we estimate N_{out} to be at least 10^4. The high-energy electrons are produced from water molecules predominantly at the nanoparticle surface, resulting in $N_{out} \approx 10^4$ as a low estimate.

From the estimated charge $Q = eN_{out}$ on the nanoparticle, the electric field at a distance r from the nanoparticle center is: $E(r) = Q/(4\pi\varepsilon_0 r^2)$, where ε_0 is the vacuum permittivity. This electric field is built after electrons leave (at the timescale of the laser pulse [65]) and before the nanoparticle hydrodynamically expands, which takes place on a timescale of few 10 ps [12, 13, 66]. Ions around the nanoparticle (either He$^+$ and He^{2+} from the gas or H$^+$ located close to the nanoparticle surface) are accelerated in this field. Their energy spectrum is [38]:

$$\frac{\mathrm{d}N}{\mathrm{d}\mathscr{E}} = \frac{16\pi^2\varepsilon_0 n}{QZe} \frac{1}{\left(\frac{1}{R_{max}} + \frac{4\pi\varepsilon_0}{QZe}\mathscr{E}\right)^4},$$
(3)

where n is the ion number density and R_{max} is the maximum ion distance from the nanoparticle. Note, that all fast ions originate from the same region and are accelerated in nearly the same field. This understanding of ion acceleration mechanism within the layer close to the nanoparticle surface is supported by theoretical calculations of the nanoplasma density evolution [67] and by CDI experiments [16, 18, 19, 22]. The CDI investigations have demonstrated an ultrafast softening of the nanoparticle surface, which means that the sharp plasma boundary at the surface of a strongly ionized nanoparticle gets softened already at the timescale of the ionizing femtosecond pulse.

Calculated He^+, He^{2+} and H^+ energy spectra together with measured averaged spectra of fast ions (same as fast 'f' peaks in figure 4(b)) are shown in figure 5(a). Due to the rather simple estimation, the measured spectral shape is not reproduced. The calculation overestimates the ion yield at lower kinetic energies due to the spherical symmetry of the model, which results in large number of ions at large distance from nanoparticle having low energy. However, this approach allows us to estimate the maximum kinetic energy that is gained by ions in the field of highly ionized nanoparticle and compare this values to experimental results.

The maximum calculated ion energy is taken as a value, for which the calculated number of ions falls below a threshold of ~5. This is a similar procedure as the experimental determination of maximum ion energies. The calculated maximum ion energies are presented in figure 5(b) together with the experimental values. The calculated ion energies are plotted versus the nanoparticle charge Q, while the experimental energies are plotted versus the fast H^+ yield that reflects the nanoparticle charging. This assumption is based on the fact that H^+ originates from the nanoparticle surface, thus the H^+ yield should reflect total charge at the nanoparticle. To get the best agreement with the experiment, we adjusted the Q axis to be in the range of $(3-7) \times 10^4 e$ and we took H^+ ions to be at a distance of 280 nm from the nanoparticle center. The choice of these parameters is in a good agreement with the estimated charging of the nanoparticle on the order of $10^4 e$ and the nanoparticle radius of 200 nm.

Accordingly, our suggested simple model explains well the observed ion energies with a small number of input parameters. Although the spectral shape cannot be reproduced well, the maximum ion energies agree with the experiment. A more advanced microscopic numerical calculation would be needed to model the measured ion spectral shape.

5. Conclusions

We have investigated acceleration of ions in plasma produced by irradiation of CsCl nanoparticles in the He gas environment with intense femtosecond XUV pulses. From analysis of electron spectra, we have followed evolution of the He microplasma in the focal volume. With increasing electron density, the shape of the electron spectrum changes significantly, evolving from individual, well resolved photolines to a broad distribution, which is characteristic for collisional interactions of electrons in a plasma. He ions get accelerated in the He plasma to kinetic energies on the order of 100 eV for He^+ and on the order of 200 eV for He^{2+}. We apply plasma sheath model to explain acceleration of ions at the microplasma-vacuum boundary. Electron plasma densities of the order of 10^{14} cm^{-3}, at which ion acceleration is observed in the current study, are comparable with the electron plasma densities used in electrical discharge plasma reactors for industrial applications [60]. This opens up an opportunity for studies of electron and ion interactions in industrial relevant plasma using femtosecond XUV pulses either produced by FELs or by laser-driven XUV sources based on high-harmonic generation [68]. The XUV flux from HHG sources can be sufficient to drive multiple ionizations in nanoscale systems [41, 69] and lead to collective autoionization [70].

In thermalized plasma containing CsCl nanoparticles, additional fraction of He^+ and He^{2+} ions with a factor of 2 higher kinetic energy have been detected. We attribute the spatial origin of these fast ions to the nanoparticle surface and explain the additional energy gain by the acceleration in the electric field around the ionized nanoparticle. Additionally, H^+ ions, with kinetic energy similar to He^+ were detected, which is attributed to the water layer at the CsCl nanoparticle surface. Thus, ions originating from the region close to the surface of the nanoparticle and ions originating from the plasma-vacuum boundary can be spectroscopically separated due to the difference in their kinetic energy. This finding, combined with our previous investigations of NIR irradiated nanoparticles in He atmosphere [38], might help to design novel pump-probe schemes to access the dynamics of core-shrinking and surface-softening in heated nanoparticles as it was observed in CDI experiments [18, 71]. Moreover, in CDI experiments at FELs, ion detection can be used for hit finding and on-line data reduction [72]. Our work shows that hits can be identified by detecting ions from the environment or H^+ from the target surface. Therefore, we believe that results of our study will contribute to further development of experimental techniques aiming on studies of plasma dynamics using intense lasers.

Data availability statement

The data cannot be made publicly available upon publication because no suitable repository exists for hosting data in this field of study. The data that support the findings of this study are available upon reasonable request from the authors.

Acknowledgments

ORCID iDs

Eva Klimešová ● https://orcid.org/0000-0002-9569-7511
Bernd Schütte ● https://orcid.org/0000-0001-5312-4611
Ulrike Frühling ● https://orcid.org/0000-0002-8423-786X
Stefan Düsterer ● https://orcid.org/0000-0003-4379-1327
Jakob Andreasson ● https://orcid.org/0000-0002-3202-2330
Maria Krikunova ● https://orcid.org/0000-0002-6152-1825

References

[1] Bostedt C, Boutet S, Fritz D M, Huang Z, Lee H J, Lemke H T, Robert A, Schlotter W F, Turner J J and Williams G J 2016 *Rev. Mod. Phys.* **88** 015007
[2] Seddon E A *et al* 2017 *Rep. Prog. Phys.* **80** 115901
[3] Young L *et al* 2018 *J. Phys. B: At. Mol. Opt. Phys.* **51** 032003
[4] Rossbach J, Schneider J R and Wurth W 2019 *Phys. Rep.* **808** 1–74
[5] Sobolev E *et al* 2020 *Commun. Phys.* **3** 97
[6] Ho P J *et al* 2020 *Nat. Commun.* **11** 167
[7] Hantke M F *et al* 2014 *Nat. Photon.* **8** 943–9
[8] van der Schot G *et al* 2015 *Nat. Commun.* **6** 5704
[9] Seibert M M *et al* 2011 *Nature* **470** 78–81
[10] Barke I *et al* 2015 *Nat. Commun.* **6** 6187
[11] Ayyer K *et al* 2021 *Optica* **8** 15–23
[12] Saalmann U 2010 *J. Phys. B: At. Mol. Opt. Phys.* **43** 194012
[13] Krikunova M *et al* 2012 *J. Phys. B: At. Mol. Opt. Phys.* **45** 105101
[14] Müller M *et al* 2015 *J. Phys. B: At. Mol. Opt. Phys.* **48** 174002
[15] Flueckiger L *et al* 2016 *New J. Phys.* **18** 043017
[16] Rupp D *et al* 2020 *Struct. Dyn.* **7** 034303
[17] Michiels R *et al* 2020 *Phys. Chem. Chem. Phys.* **22** 7828–34
[18] Gorkhover T *et al* 2016 *Nat. Photon.* **10** 93–97
[19] Nishiyama T *et al* 2019 *Phys. Rev. Lett.* **123** 123201
[20] Tachibana T *et al* 2015 *Sci. Rep.* **5** 10977
[21] Kumagai Y *et al* 2018 *Phys. Rev. X* **8** 031034
[22] Niozu A *et al* 2021 *Phys. Rev. X* **11** 031046
[23] Wabnitz H *et al* 2002 *Nature* **420** 482–5
[24] Bostedt C *et al* 2008 *Phys. Rev. Lett.* **100** 133401
[25] Rupp D *et al* 2016 *Phys. Rev. Lett.* **117** 153401
[26] Gorkhover T *et al* 2012 *Phys. Rev. Lett.* **108** 245005
[27] Di Cintio P, Saalmann U and Rost J M 2013 *Phys. Rev. Lett.* **111** 123401
[28] Iwan B *et al* 2012 *Phys. Rev. A* **86** 033201
[29] Ovcharenko Y *et al* 2014 *Phys. Rev. Lett.* **112** 073401
[30] Oelze T *et al* 2017 *Sci. Rep.* **7** 40736
[31] LaForge A C *et al* 2021 *Phys. Rev. X* **11** 021011
[32] Asmussen J D *et al* 2022 *J. Phys. Chem. Lett.* **13** 4470–8
[33] Buchta D *et al* 2013 *J. Chem. Phys.* **139** 084301
[34] Ltaief L B, Shcherbinin M, Mandal S, Krishnan S R, Richter R, Pfeifer T and Mudrich M 2020 *J. Phys. B: At. Mol. Opt. Phys.* **53** 204001
[35] Hantke M F *et al* 2018 *IUCrJ* **5** 673–80
[36] Roth N, Awel S, Horke D A and Küpper J 2018 *J. Aerosol Sci.* **124** 17–29
[37] Bielecki J *et al* 2019 *Sci. Adv.* **5** eaav8801
[38] Klimešová E, Kulyk O, Dittrich L, Andreasson J and Krikunova M 2021 *Phys. Rev. A* **104** L061101
[39] Klimešová E, Kulyk O, Gu Y, Dittrich L, Korn G, Hajdu J, Krikunova M and Andreasson J 2019 *Sci. Rep.* **9** 8851
[40] Krikunova M, Maltezopoulos T, Wessels P, Schlie M, Azima A, Wieland M and Drescher M 2011 *J. Chem. Phys.* **134** 024313
[41] Schütte B, Campi F, Arbeiter M, Fennel T, Vrakking M J J and Rouzée A 2014 *Phys. Rev. Lett.* **112** 253401

[42] Krikunova M, Maltezopoulos T, Wessels P, Schlie M, Azima A, Gaumnitz T, Gebert T, Wieland M and Drescher M 2012 *Phys. Rev. A* **86** 043430
[43] Niozu A *et al* 2022 *Phys. Rev. A* **106** 043116
[44] Tiedtke K *et al* 2009 *New J. Phys.* **11** 023029
[45] Oelze T *et al* 2020 *Opt. Express* **28** 20686–703
[46] DePonte D P, Weierstall U, Schmidt K, Warner J, Starodub D, Spence J C H and Doak R B 2008 *J. Phys. D* **41** 195505
[47] Ewing G E and Peters S J 1997 *Surf. Rev. Lett.* **04** 757–70
[48] Peters S J and Ewing G E 1997 *J. Phys. Chem. B* **101** 10880–6
[49] Arsic J, Kaminski D M, Radenovic N, Poodt P, Graswinckel W S, Cuppen H M and Vlieg E 2004 *J. Chem. Phys.* **120** 9720–4
[50] Fruehling U *et al* 2009 *Nat. Photon.* **3** 523–8
[51] Bizau J and Wuilleumier F 1995 *J. Electron Spectrosc. Relat. Phenom.* **71** 205–24
[52] Wehlitz R *et al* 1997 *J. Phys. B: At. Mol. Opt. Phys.* **30** L51–L58
[53] Lindle D W, Ferrett T A, Becker U, Kobrin P H, Truesdale C M, Kerkhoff H G and Shirley D A 1985 *Phys. Rev. A* **31** 714–26
[54] Thompson D B, Bolognesi P, Coreno M, Camilloni R, Avaldi L, Prince K C, de Simone M, Karvonen J and King G C 1998 *J. Phys. B: At. Mol. Opt. Phys.* **31** 2225–38
[55] Banna M S, McQuaide B H, Malutzki R and Schmidt V 1986 *J. Chem. Phys.* **84** 4739–44
[56] Verna A *et al* 2020 *New J. Phys.* **22** 123029
[57] Kim Y K and Rudd M E 1994 *Phys. Rev. A* **50** 3954–67
[58] Wabnitz H, de Castro A R B, Gürtler P, Laarmann T, Laasch W, Schulz J and Möller T 2005 *Phys. Rev. Lett.* **94** 023001
[59] Roth J R 1995 *Industrial Plasma Engineering vol 1: Principles* (Institute of Physics Publishing)
[60] Lieberman M A and Lichtenberg A J 2005 *Principles of Plasma Discharges and Materials Processing* (Wiley)
[61] Yeh J and Lindau I 1985 *At. Data Nucl. Data tables* **32** 1–155
[62] Osmekhin S, Huttula M, Urpelainen S, Aksela H and Aksela S 2008 *J. Phys. B: At. Mol. Opt. Phys.* **41** 035006
[63] Moise A, Alagia M, Avaldi L, Feyer V, Prince K C and Richter R 2010 *J. Phys. B: At. Mol. Opt. Phys.* **43** 215001
[64] Arbeiter M and Fennel T 2010 *Phys. Rev. A* **82** 013201
[65] Oelze T *et al* 2019 *Phys. Rev. A* **99** 043423
[66] Rath A D *et al* 2014 *Opt. Express* **22** 28914–25
[67] Peltz C, Varin C, Brabec T and Fennel T 2014 *Phys. Rev. Lett.* **113** 133401
[68] Klimešová E *et al* 2021 *Eur. Phys. J. Spec. Top.* **230** 4183–94
[69] Schütte B, Arbeiter M, Fennel T, Vrakking M J J and Rouzée A 2014 *Phys. Rev. Lett.* **112** 073003
[70] Jurkovičová L *et al* 2024 *Commun. Phys.* **7** 26
[71] Bacellar C *et al* 2022 *Phys. Rev. Lett.* **129** 073201
[72] Andreasson J *et al* 2014 *Opt. Express* **22** 2497–510